

# New physics at nuSTORM

Kaustav Chakraborty,<sup>1,2,\*</sup> Srubabati Goswami,<sup>1,†</sup> and Kenneth Long<sup>3,4,‡</sup>

<sup>1</sup>*Theoretical Physics Division, Physical Research Laboratory, Ahmedabad - 380009, India*

<sup>2</sup>*Discipline of Physics, Indian Institute of Technology, Gandhinagar - 382355, India*

<sup>3</sup>*Department of Physics, Imperial College London, Exhibition Road, SW7 2AZ, UK*

<sup>4</sup>*STFC Rutherford Appleton Laboratory,  
Harwell Campus, Didcot, OX11 0QX, UK*

In this work we investigate the usefulness of nuSTORM as a probe of two new-physics scenarios which are sterile neutrinos and non-unitarity of the neutrino mixing matrix. For the sterile neutrino we show the importance of the neutral current events when combined with the charged current events to constrain the effective mixing angle,  $\theta_{\mu\mu}$ , and the sterile mixing angles  $\theta_{14}$  and  $\theta_{24}$ . We also study the role nuSTORM will play in the study of neutrino oscillation physics if the three generation neutrino mixing matrix is non-unitary. In this context we elucidate the role of nuSTORM, considering both charged current and neutral current events, in constraining the various non-unitarity parameters such as  $\alpha_{11}$ ,  $|\alpha_{21}|$  and  $\alpha_{22}$ .

---

\* Email Address: [kaustav@prl.res.in](mailto:kaustav@prl.res.in)

† Email Address: [sruba@prl.res.in](mailto:sruba@prl.res.in)

‡ Email Address: [k.long@imperial.ac.uk](mailto:k.long@imperial.ac.uk)

## I. INTRODUCTION

Neutrino oscillation experiments have conclusively established the paradigm of the three-flavour neutrino oscillations and oscillation parameters are being determined with increasing precision. The three parameters that are yet to be determined are the mass hierarchy, the octant of the atmospheric mixing angle,  $\theta_{23}$ , and the leptonic CP phase,  $\delta_{CP}$ . There are some indications of the value of these parameters from the current data. Future planned/proposed high statistics experiments are expected to clinch these issues. With the determination of the three-neutrino mixing parameters already on the horizon, efforts have been made to explore new physics beyond the Standard Model in these experiments. New physics scenarios that have garnered considerable interest in the community include light sterile neutrinos, non-unitarity of the neutrino mixing matrix, non-standard interactions of the neutrinos etc.

The existence of light sterile neutrinos was postulated to explain the LSND results [1, 2]. LSND reported signals of  $\nu_\mu - \nu_e$  oscillations with mass-squared difference of the order of  $\text{eV}^2$ . This was supported by MiniBooNE [3, 4] and also by the gallium and reactor anomalies [5–7]. In order to accommodate the  $\text{eV}^2$  oscillation scale the simplest possibility is to add a sterile neutrino to the Standard Model. There are two possible ways this can be done. (i) The 2+2 scenario in which the oscillation to sterile neutrino constitute the dominant solution either to solar or atmospheric neutrino anomaly and disfavoured from current data [8]. (ii) The 3+1 or 1+3 picture in which the sterile neutrino is separated by an  $\text{eV}^2$  mass difference from the 3 active states [9]. 3+1 (1+3) corresponds to the 3 active states to be lighter (heavier). Cosmological constraints on sum of neutrino masses pose a serious challenge in accommodating an  $\text{eV}$  scale sterile neutrino scenario. To address these, secret neutrino interactions [10] or lower reheating temperature [11–13] which can is the 1+3 picture is more disfavoured from cosmology since there are three heavier states. The 3+1 picture can provide an acceptable fit to the data [14, 15] albeit the tension between disappearance and appearance data.

There are several new experiments planned to test the sterile neutrino hypothesis[16–23]. It was realized recently that beam-based long-baseline experiments can also probe the parameter space of the sterile neutrino models and several studies have been carried out in

this direction considering the current as well as proposed experiments. Future experiments such as DUNE[24] or T2HK[25] are high statistics experiments and therefore the systematics are expected to play a crucial role, one of the major sources of systematic uncertainty are the neutrino-nucleus interaction cross-sections. Neutrinos from Stored Muons (nuSTORM)[21, 22] is a facility proposed for the measurement of neutrino-nucleus cross-sections with percent-level precision. The high precision can be achieved because the stored-muon beam will allow the determination of neutrino flux with high accuracy. It has been shown that nuSTORM has excellent capability to search for the existence of light sterile neutrinos of the type postulated to explain the LSND and MiniBooNE results [1–4].

Beyond the Standard Model (BSM) physics descriptions have become essential in describing the non-zero neutrino mass after the discovery of neutrino oscillations. Non-zero neutrino masses can be generated by the “see-saw” mechanism through an effective lepton number violating dimension-five operator of the form  $LL\phi\phi$  which can be derived from physics beyond the Standard Model [26, 27]. Such BSM physics can also lead to non-unitarity of the neutrino mixing matrix[28–36]. The unitarity of the PMNS matrix can be tested in accelerator-based neutrino oscillation experiments. Several studies have been performed to understand the implications of non-unitarity in present and future long baseline experiments [37–40]. In this context nuSTORM also holds promise for the study of the non-unitarity of the PMNS matrix and the constraint of the parameters which generate non-unitarity in the PMNS sector.

The neutrino beam in nuSTORM originates from the muon decay process:  $\mu^+ \rightarrow e^+ \nu_e \bar{\nu}_\mu$  with 50%  $\nu_e$  and 50%  $\bar{\nu}_\mu$  which can give  $e^-$  and  $\mu^+$  at the detectors in absence of oscillation or any other new physics. If however there are flavour-changing processes then one can get wrong sign leptons which can constitute smoking-gun signals of new physics. A detector with charge identification capability is therefore ideal.

The sterile neutrino analysis performed in [41] considered a magnetized iron-calorimeter detector with a superior efficiency to identify the charge of the muons. This gives the detector the ability to record the  $\mu^-$  events originating from  $P_{\nu_e \nu_\mu}$  oscillations along with the  $\mu^+$  coming from the  $P_{\bar{\nu}_\mu \bar{\nu}_\mu}$  channel. In this analysis only the charged current events were considered. However, there are also a large number of neutral current (NC) events. In a three-

flavour-mixing paradigm, given the flavour universality of the neutral current interactions and  $P_{\mu e} + P_{\mu\mu} + P_{\mu\tau} = 1$ , NC events are not sensitive to the oscillation parameters. However, in the presence of new physics this may not be the case. For instance, for oscillations of muon neutrinos to a sterile neutrino, the rate of neutral-current events will be multiplied by  $(1 - P_{\mu s})$ . The usefulness of NC events for sterile neutrino searches in the context of beam experiments has been studied in [42–45].

In this article we present the capabilities of nuSTORM in some sterile neutrino searches as well as the search for non-unitarity of the neutrino mixing matrix. In section:II we discuss the nuSTORM proposal and the simulation of the facility. We discuss the results obtained in our study in section:III, where subsection:III A focuses on the study of sterile neutrinos at nuSTORM, while the consideration of the non-unitarity of the neutrino mixing is presented in subsection:III B. Conclusions are presented in section:IV.

## II. DETAILS OF SIMULATION

We follow the configuration and detector simulations from [21, 22, 46]. The unoscillated flux was taken from [21]. The simulation has been performed using the General Long Baseline Experiment Simulator (GLOBES) package[47, 48]. The flux is based on the decay  $\mu^+ \rightarrow e^+ + \nu_e + \bar{\nu}_\mu$ . The neutrino beam is generated with 50 GeV protons with  $2 \times 10^{21}$  protons on target over the duration of 10 years. Pions of 5 GeV are injected into the muon storage ring. Muons with energy of the order 3.8 GeV subsequently decay to give  $\nu_e$  and  $\bar{\nu}_\mu$ . The  $\nu_e$  flux peaks at 2.5 GeV whereas the  $\bar{\nu}_\mu$  flux peaks at 3 GeV. nuSTORM is simulated as described in [21, 22].

In our simulation we consider a far detector at a distance of 2 km from the source unless otherwise mentioned. A 1.3 kt magnetized iron-scintillator calorimeter has been selected as the detector for short-baseline oscillation physics at nuSTORM as it has excellent charge selection and detection characteristics for muons. Therefore, the important channels for this experiment are  $\nu_e \rightarrow \nu_\mu$  appearance channel and  $\bar{\nu}_\mu \rightarrow \bar{\nu}_\mu$  disappearance channel. The

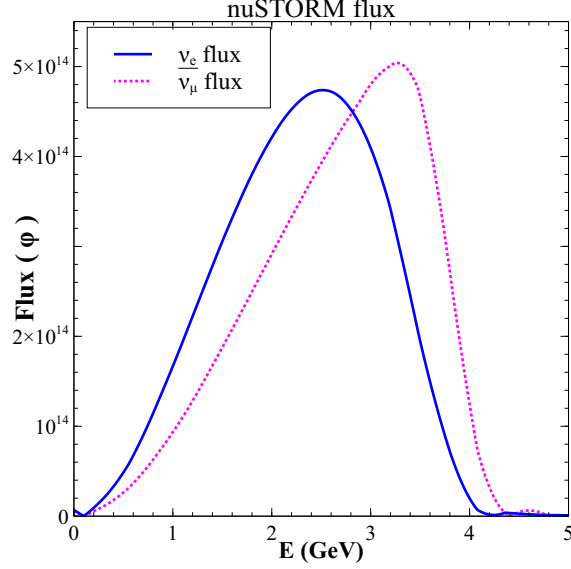


FIG. 1: The unoscillated  $\nu_e$  and  $\bar{\nu}_\mu$  flux extracted from the storage ring. The flux is evaluated for  $(3.8 \pm 0.38)$  GeV/c muon decay at a distance of 2 km[21].

number of events in the  $i^{th}$  energy bin are calculated as

$$n_\alpha^i = \frac{N}{L^2} \int_{E_i - \frac{\Delta E_i}{2}}^{E_i + \frac{\Delta E_i}{2}} dE' \int_0^\infty \varepsilon(E) \phi_\beta(E) P_{\alpha\beta}(E) \sigma_\alpha(E) R^c(E, E') \varepsilon^c(E') dE \quad (1)$$

where,  $E$  denotes the true neutrino energy and  $E'$  denotes the measured neutrino energy.  $R^c(E, E')$  denotes the smearing matrix, which relates the true and the measured energy. This includes both kinematic smearing and the smearing due to energy reconstruction. This is often taken as a Gaussian. Migration matrices that give the probability for a neutrino generated in the  $i^{th}$  energy bin to be reconstructed in the  $j^{th}$  energy bin, if available from detector simulations, can also be used.  $\varepsilon^c(E')$  denotes the post-smearing efficiency which contains, for instance, the information on energy cuts used.  $\varepsilon(E)$  denotes the pre-smearing efficiency.

In our analysis we have taken the energy resolution as a Gaussian. With  $R^c(E, E') = \frac{1}{\sigma(E)\sqrt{2\pi}} e^{-\frac{(E-E')^2}{2\sigma^2(E)}}$  and  $\sigma(E) = 0.15E$ . The energy cuts are incorporated as “post smearing efficiencies” as follows:

$$\varepsilon^c(E') = 0 \quad ; \quad 0 < E' < 1 \quad (2)$$

$$\varepsilon^c(E') = 1 \quad ; \quad E' > 1 \quad (3)$$

The event rates at the detector (multiplied by the efficiencies) and the corresponding pre-smearing efficiencies are given in table I and the unoscillated flux is given in fig.1.

Channel	$N_{events}$	Efficiency at the detector
$\nu_e \rightarrow \nu_\mu$ CC	61	0.18
$\nu_e \rightarrow \nu_e$ CC	39865	0.18
$\bar{\nu}_\mu \rightarrow \bar{\nu}_\mu$ NC	8630	0.18
$\bar{\nu}_\mu \rightarrow \bar{\nu}_\mu$ CC	114983	0.94
$\nu_e \rightarrow \nu_e$ NC	13605	0.18

TABLE I: The events observed at the detector, this is equal to the expected number of events at the detector multiplied by their efficiencies according to [21, 22].

The impact of the neutral current events is evaluated using a  $\chi^2$  which is defined as

$$\chi_{tot}^2 = \min_{\xi, \omega} \left\{ \sum_r (\chi_{stat}^2(\omega, \xi) + \chi_{pull}^2(\xi))_r \right\}. \quad (4)$$

r denotes the “rules” and the statistical  $\chi^2$  is  $\chi_{stat}^2$ , systematic uncertainties are incorporated by  $\chi_{pull}^2$  calculated by the method of pulls with pull variables  $\xi$ . The significance over each rule is calculated separately and the total  $\chi^2$  is calculated by summation over all the various rules. Each “rule” signifies a different channel. The total  $\chi^2$  is marginalized over the oscillation parameters. The relevant oscillation parameters are represented by  $\omega$ . The statistical  $\chi_{stat}^2$  is calculated assuming Poisson distribution,

$$\chi_{stat}^2 = \sum_i 2 \left( N_i^{test} - N_i^{true} - N_i^{true} \log \frac{N_i^{test}}{N_i^{true}} \right). \quad (5)$$

Here, ‘i’ stands for the number of bins and  $N_i^{test}, N_i^{true}$  stands for total number of test and true events respectively. To include the effects of systematics in  $N_i^{test}$ , the normalization and energy calibration errors are parametrized using the “pull” and “tilt” variables respectively. These are incorporated as follows:

$$N_i^{(k)test}(\omega, \xi) = \sum_{k=s,b} N_i^{(k)}(\omega) \left[ 1 + c_i^{(k)norm} \xi^{(k)norm} + c_i^{(k)tilt} \xi^{(k)tilt} \frac{E_i - \bar{E}}{E_{max} - E_{min}} \right], \quad (6)$$

where  $k = s(b)$  represent the signal (background) events. The effect of the pull variable  $\xi^{norm}(\xi^{tilt})$  on the number of events is denoted by  $c_i^{norm}(c_i^{tilt})$ . The bin-by-bin mean reconstructed energy is represented by  $E_i$  where  $i$  represents the bin.  $E_{min}$ ,  $E_{max}$  and  $\bar{E} = (E_{max} + E_{min})/2$  are the minimum energy, maximum energy and the mean energy over this range.

The signal(background) normalization uncertainty for the appearance channel is taken as 1%(10%) [21, 22] while for  $\nu_{\bar{\mu}}$  channel they are kept at 5%(10%). For NC the signal and background errors are taken to be 5% and 10% respectively. A background rejection factor of  $10^{-3}$  is used for the disappearance channel while  $10^{-5}$  is used for appearance channel [21, 22]. For NC events we use a background rejection factor of  $10^{-4}$ . We have checked that the  $\chi^2$  does not depend significantly on the background rejection factor for the NC analysis. The unoscillated events observed at the detector have been shown in the fig.2.

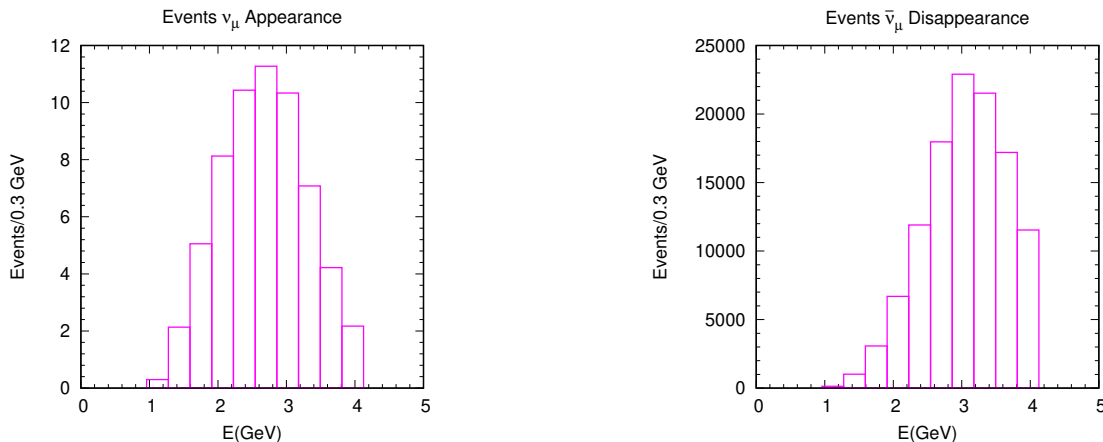


FIG. 2: The figure shows the distribution of events observed in absence of oscillation. A bin with bin width of 0.3 GeV. The left plot shows the appearance events while the right is for the disappearance events.

Data is generated assuming the standard three-neutrino oscillations scenario as the null hypothesis and the new physics scenario under study is used as the alternative hypothesis. Schematically the number of events in the different channels can be written as

Oscillation parameters	Value considered to simulate nuSTORM
$\sin^2 \theta_{13}$	0.022
$\sin^2 \theta_{12}$	0.31
$\sin^2 \theta_{23}$	0.558
$\Delta m_{21}^2$ (eV <sup>2</sup> )	$7.39 \times 10^{-5}$
$ \Delta m_{31}^2 $ (eV <sup>2</sup> )	$2.52 \times 10^{-3}$
$\delta$	0°
$\sin^2 \theta_{14}$	0.025
$\sin^2 \theta_{24}$	0.0023
$\Delta m_{41}^2$ (eV <sup>2</sup> )	0.89

TABLE II: The values of the 3 neutrino oscillation parameters [49, 50] and the representative values for 3+1 neutrino mixing [14] used in the present analysis.

$$N_{\mu}^{CC} = \Phi(\nu_e)P_{e\mu}\sigma_{CC} \quad (7)$$

$$N_{\bar{\mu}}^{CC} = \Phi(\bar{\nu}_{\mu})P_{\bar{\mu}\bar{\mu}}\sigma_{CC} \quad (8)$$

$$N_{total}^{NC} = \Phi(\bar{\nu}_{\mu})(1 - P_{\mu s})\sigma_{NC} + \Phi(\nu_e)(1 - P_{es})\sigma_{NC} \quad (9)$$

### III. RESULTS AND DISCUSSIONS

#### A. Sterile Neutrino

Since we are considering a distance of  $\sim 2$  km and  $E \sim 3$  GeV there can be oscillations governed by a mass-squared difference of order eV<sup>2</sup>. Other terms do not contribute since the oscillation wavelengths are much larger. Thus we have the ‘‘One Mass Scale Dominance’’ (OMSD) approximation in which the oscillation probabilities can be cast into an effective two flavor form. For the 3+1 picture, under the OMSD approximation, one has

$$P_{\alpha,\beta} = 4|U_{\alpha 4}|^2|U_{\beta 4}|^2 \sin^2 \left( \frac{\Delta m_{41}^2 L}{4E} \right) \quad (10)$$

and,

$$P_{\alpha\alpha} = 1 - 4|U_{\alpha 4}|^2(1 - |U_{\alpha 4}|^2) \sin^2 \left( \frac{\Delta m_{41}^2 L}{4E} \right) \quad (11)$$

Bounds on individual mixing angles are derived using the parametrization

$$U = R_{34}\tilde{R}_{24}\tilde{R}_{14}R_{23}\tilde{R}_{13}R_{12}. \quad (12)$$

Since we are in an effective two-generation approximation, the phases do not appear in the oscillation probabilities and ignoring them one has,

$$\begin{aligned} U_{e4} &= \sin \theta_{14} \\ U_{\mu 4} &= \cos \theta_{14} \sin \theta_{24} \\ U_{\tau 4} &= \cos \theta_{14} \sin \theta_{24} \\ U_{s4} &= \cos \theta_{14} \cos \theta_{24} \cos \theta_{34} \end{aligned} \quad (13)$$

The relevant oscillation probabilities are given as

$$P_{e\mu} = 4 \cos^2 \theta_{14} \sin^2 \theta_{14} \sin^2 \theta_{24} \sin^2 \left( \frac{\Delta m_{41}^2 L}{4E} \right) \quad (14)$$

$$P_{\mu\mu} = 1 - 4 \sin^2 \theta_{24} \cos^2 \theta_{14} (1 - \sin^2 \theta_{24} \cos^2 \theta_{14}) \sin^2 \left( \frac{\Delta m_{41}^2 L}{4E} \right) \quad (15)$$

$$P_{\mu s} = 4 \cos^4 \theta_{14} \cos^2 \theta_{24} \cos^2 \theta_{34} \sin^2 \theta_{24} \sin^2 \left( \frac{\Delta m_{41}^2 L}{4E} \right) \quad (16)$$

$$P_{es} = 4 \cos^2 \theta_{14} \sin^2 \theta_{14} \cos^2 \theta_{24} \cos^2 \theta_{34} \sin^2 \left( \frac{\Delta m_{41}^2 L}{4E} \right) \quad (17)$$

$$\sin^2 2\theta_{\mu e} = 4|U_{e4}|^2|U_{\mu 4}|^2 = 4s_{14}^2 c_{14}^2 s_{24}^2 \quad (18)$$

$$\sin^2 2\theta_{\mu\mu} = 4|U_{\mu 4}|^2(1 - |U_{\mu 4}|^2) = 4c_{14}^2 s_{24}^2 (1 - c_{14}^2 s_{24}^2) \quad (19)$$

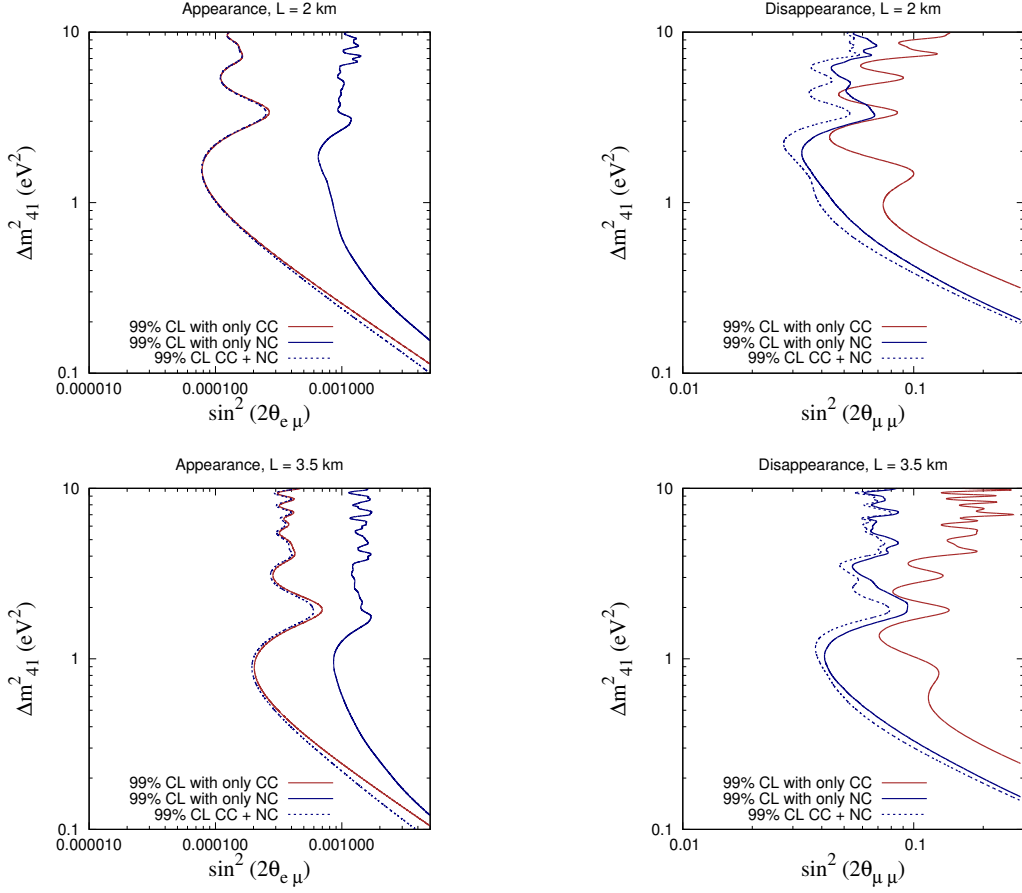


FIG. 3: The testable regions for sterile neutrinos as predicted by nuSTORM in terms of  $\Delta m_{41}^2$  vs  $\sin^2 \theta_{\mu e}$  for the left plots and  $\Delta m_{41}^2$  vs  $\sin^2 \theta_{\mu\mu}$  for the right. The first row indicates the sensitivities or baseline of 2 km while the second row for 3.5 km. Each plot consists of 3 contours of 99% confidence level significance exclusion regions for various channels as labeled in the plots.

Figure 3 shows the bounds on  $\Delta m_{41}^2$  with respect to the effective mixing angles  $\theta_{\mu e}$  and  $\theta_{\mu\mu}$  for baselines of 2 km and 3.5 km. The oscillation amplitudes satisfy:  $P_{e\mu} \propto s_{14}^2 s_{24}^2$ ;  $P_{\mu\mu} \propto 1 - s_{24}^2$ ; and  $P_{es} + P_{\mu s} \propto s_{14}^2 + s_{24}^2$  (see eq.14 - 17). Therefore, in the case of the appearance channel,  $P_{e\mu}$  can constrain the effective mixing angle  $\sin^2 2\theta_{\mu e}$  which is a product of  $s_{14}^2 s_{24}^2$  while the neutral-current channel cannot constrain the product of  $s_{14}^2 s_{24}^2$  and hence cannot efficiently constrain  $\sin^2 2\theta_{\mu e}$ . The disappearance channel effectively probes the parameter  $\theta_{\mu\mu}$  in terms of the parameter  $s_{24}^2$ , also the neutral current channel probes  $s_{14}^2 + s_{24}^2$ , hence, the neutral current channel can significantly constrain the parameter  $\theta_{\mu\mu}$ .

The 2 km baseline was chosen for comparison to the results presented in [51]. The choice of the 3.5 km baseline was motivated by the fact that this places the detector at oscillation maxima for  $\Delta m_{41}^2 \sim 1\text{eV}^2$ . If we study the bottom panel of the fig.3 we observe that the best sensitivities for both  $\theta_{\mu e}$  and  $\theta_{\mu\mu}$  are observed around  $\Delta m_{41}^2 \sim 1\text{eV}^2$ , which is expected. Proceeding to the top panel of the fig.3 we find that the most sensitive region has shifted to  $\Delta m_{41}^2 \sim 1.2\text{eV}^2$ , this is expected because  $\Delta m_{41}^2 L \approx 3.7\text{eV}^2\text{km}$ . However, the overall sensitivity is better for the lower baseline of 2 km as the lower baseline has a lower statistical uncertainty because of a higher flux at the detector.

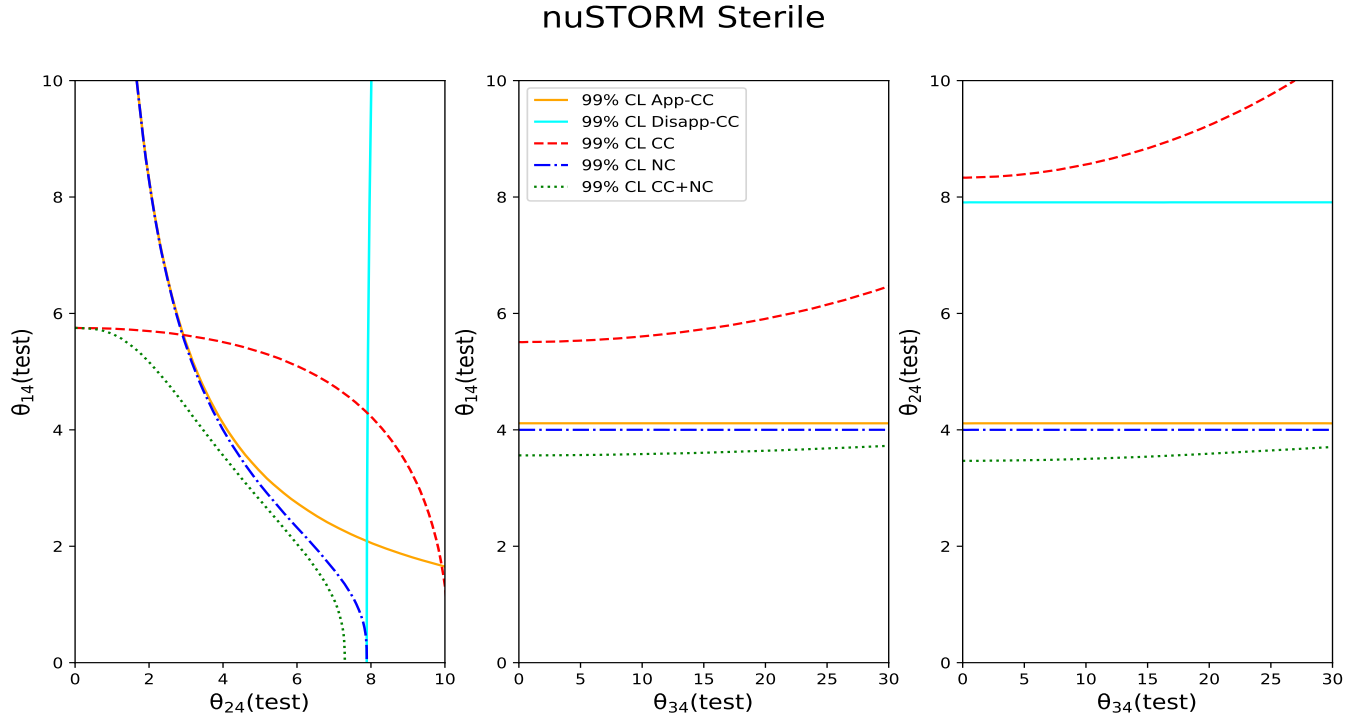


FIG. 4: The testable regions for sterile neutrinos at nuSTORM for  $\Delta m_{41}^2 = 1\text{eV}^2$  and baseline of 2 km in terms of  $\theta_{14}$ ,  $\theta_{24}$  and  $\theta_{34}$  bounds. The first, second and third plots present the  $\theta_{14}(\text{test})$  vs  $\theta_{24}(\text{test})$ ,  $\theta_{14}(\text{test})$  vs  $\theta_{34}(\text{test})$  and  $\theta_{24}(\text{test})$  vs  $\theta_{34}(\text{test})$  contours respectively. Each plot consists of 5 contours of 99% confidence level significance exclusion regions for various channels as labeled in the plots.

Figure 4 presents the predicted  $\theta_{14}$ ,  $\theta_{24}$  and  $\theta_{34}$  bounds expected from nuSTORM. The first plot from fig.4 shows the  $\theta_{14}$  versus  $\theta_{24}$  exclusion region considering the data generated from 3 flavour oscillation with parameters as given in tab:I, but setting the fourth generation parameters to zero. The solid orange line shows the  $\theta_{14}$  versus  $\theta_{24}$  exclusion region predicted from the appearance channel, the relevant probability for this channel is  $P_{e\mu}$  given by the expression in eq:14. As, the allowed regions for  $\theta_{14}$ ,  $\theta_{24}$  are small hence the expression for  $P_{e\mu}$  at constant energy and baseline is roughly  $\propto \theta_{14}^2 \theta_{24}^2$  which explains the hyperbolic nature of the charged current appearance plot. The disappearance probability  $P_{\bar{\mu}\bar{\mu}}$  approximately reduces to  $1 - 4\theta_{24}^2$ , which is independent of  $\theta_{14}$ , so  $\theta_{14}$  remains unaffected by the disappearance channel. Another important channel which can be probed is the neutral-current channel. The total contribution to the neutral-current channel comes from  $P_{\mu s} + P_{es}$  because neutral-current events from neutrino and antineutrino cannot be differentiated by the detector. The total neutral-current probability approximately reduces to  $P_{\mu s} + P_{es} \propto \theta_{14}^2 + \theta_{24}^2$ , which describes the approximate elliptical nature of the neutral current channel given by red dashed lines in the fig:4. The total CC event curve(blue dashed curve) is the total contribution of appearance CC and disappearance CC. While the green dotted curve presents the contribution of all the above channels i.e. the total CC and NC event samples. It is clear from the figure that the inclusion of NC events can put stringent bounds on both  $\theta_{14}$  and  $\theta_{24}$ . We can conclude from this study that nuSTORM will be able to test  $\theta_{14}$ ,  $\theta_{24}$  up to  $6^\circ$  and  $7.5^\circ$  respectively. Comparing the results obtained with the expected sensitivity of DUNE [52] it was found that neutral current events from DUNE can resolve  $\theta_{14}$  up to  $10^\circ$  and  $\theta_{24}$  upto  $15^\circ$  with 5% systematics for  $\Delta m_{41}^2 = 0.5\text{eV}^2$ .

The second and third plots in the figure show the ability of nuSTORM to constrain  $\theta_{14}$  and  $\theta_{24}$  with respect to  $\theta_{34}$ . Taking all the channels into account both  $\theta_{14}$  and  $\theta_{24}$  can be approximately constrained up to  $4^\circ$  at nuSTORM. In both the plots it is clear that the charged current interactions are independent of  $\theta_{34}$  which is also understood from the expressions for  $P_{e\mu}$  and  $P_{\bar{\mu}\bar{\mu}}$ . The only dependence on  $\theta_{34}$  can come from the neutral current channel. However,  $P_{e\mu} + P_{\bar{\mu}\bar{\mu}} \propto \cos^2 \theta_{34}$ , as a result of which there is weak dependence of  $\theta_{34}$  on the neutral current events hence  $\theta_{34}$  cannot be constrained by neutral current events in nuSTORM.

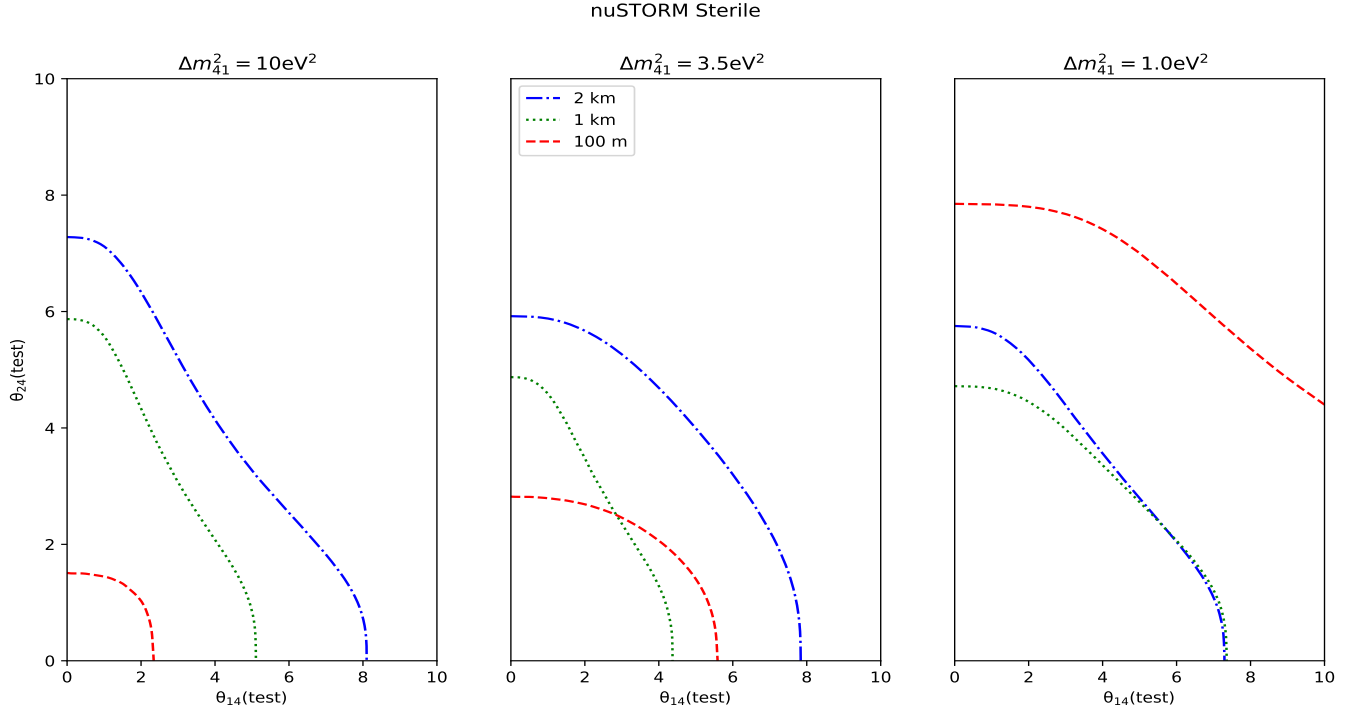


FIG. 5: The testable regions for sterile neutrinos at nuSTORM in terms of  $\theta_{14}$  vs  $\theta_{24}$  bounds. The first plot presents the  $\theta_{14}(\text{test})$  vs  $\theta_{24}(\text{test})$  for  $\Delta m_{41}^2 = 1\text{eV}^2$ , the second plot for  $\Delta m_{41}^2 = 3.5\text{eV}^2$  and the third plot for  $\Delta m_{41}^2 = 10\text{eV}^2$ . Each plot consists of 3 contours of 99% confidence level significance exclusion regions for various baselines as labeled in the plots.

The left plot in fig:5 shows the effect of varying the baseline of nuSTORM on the bounds in the  $\theta_{14}$ ,  $\theta_{24}$  plane for  $\Delta m_{41}^2 = 1\text{eV}^2$ . The best sensitivity of an experiment is observed at the oscillation maxima. The first oscillation maximum is given by  $1.27\Delta m_{41}^2 L/E = \pi/2$ . As the mean energy of the experiment is  $\sim 3$  GeV,  $\Delta m_{41}^2 L \approx 3.7\text{eV}^2$  km. It is evident from the relation that probing a larger  $\Delta m_{41}^2$  requires a smaller baseline( $L$ ) and vice versa. Analyzing the red curves in the fig:5, which show result for a the baseline of 100 m, we observe that as  $\Delta m_{41}^2$  is increased the sensitivity also increases. Similarly, if we observe the green curves representing a 1 km baseline, we observe that the best sensitivity is obtained for the case  $\Delta m_{41}^2 = 3.5 \text{eV}^2$  which is expected from the above relation. Deviation from  $\Delta m_{41}^2 = 3.5\text{eV}^2$ ,

on either side compromises the sensitivity. The blue curves demonstrate the sensitivities of the 2 km baseline for nuSTORM. The  $\Delta m_{41}^2 \approx 1.8\text{eV}^2 \text{ km}$  is expected to have the best sensitivity for the 2 km baseline. As we increase the  $\Delta m_{41}^2$  gradually the sensitivity decreases with increasing  $\Delta m_{41}^2$ . We observe that the 1 km baseline has good sensitivity for both  $\theta_{14}$  and  $\theta_{24}$  consistently over the range of  $\Delta m_{41}^2$ .

## B. Non-Unitarity

In presence of non unitarity, the time evolution of the mass eigenstate in vacuum is:

$$i\frac{d}{dt}|\nu_i\rangle = H|\nu_i\rangle, \quad (20)$$

where  $H$  is the Hamiltonian in the mass basis. After time  $t(\equiv L)$ , the flavour state can be written as

$$|\nu_\alpha(t)\rangle = N_{\alpha i}^*|\nu_i(t)\rangle = N_{\alpha i}^*(e^{-iHt})_{ij}|\nu_j(t=0)\rangle. \quad (21)$$

In this framework the mixing matrix  $N$  can be parametrized as:

$$N = N^{NP}U = \begin{bmatrix} \alpha_{11} & 0 & 0 \\ \alpha_{21} & \alpha_{22} & 0 \\ \alpha_{31} & \alpha_{32} & \alpha_{33} \end{bmatrix} U; \quad (22)$$

where  $U$  is the PMNS matrix,  $N^{NP}$  is the left triangle matrix which parametrizes the non unitarity. In the matrix  $N^{NP}$  the diagonal elements are real and the off diagonal elements can be complex.

The above discussions leads us to the transition probability:

$$P(\nu_\alpha \rightarrow \nu_\beta) = |\langle \nu_\beta | \nu_\alpha(t) \rangle|^2 = |N_{\alpha i}^* \text{diag}(e^{-i\Delta m_{i1}^2 t/2E})_{ij} N_{\beta j}|^2 \quad (23)$$

Using the above parametrization the transition probabilities  $P_{\mu e}$  and  $P_{\mu\mu}$  can be written:

$$\begin{aligned} P_{e\mu} = & \alpha_{11}^2 |\alpha_{21}|^2 - 4 \sum_{j>i}^3 \text{Re} [N_{\mu j}^* N_{e j} N_{\mu i} N_{e i}^*] \sin^2 \left( \frac{\Delta m_{ji}^2 L}{4E} \right) \\ & + 2 \sum_{j>i}^3 \text{Im} [N_{\mu j}^* N_{e j} N_{\mu i} N_{e i}^*] \sin \left( \frac{\Delta m_{ji}^2 L}{2E} \right). \end{aligned} \quad (24)$$

$$P_{\mu\mu} = (|\alpha_{21}|^2 + \alpha_{22}^2)^2 - 4 \sum_{j>i}^3 |N_{\mu j}|^2 |N_{\mu i}|^2 \sin^2 \left( \frac{\Delta m_{ji}^2 L}{4E} \right). \quad (25)$$

For nuSTORM, with a baseline of 2 km, the transition probabilities become independent of the baseline length because  $\frac{\Delta m^2 L}{E} \ll 1$ . Therefore, the relevant transition probabilities are:

$$P_{e\mu} = \alpha_{11}^2 |\alpha_{21}|^2, \text{ and} \quad (26)$$

$$P_{\mu\mu} = (|\alpha_{21}|^2 + \alpha_{22}^2)^2 \quad (27)$$

Along with the charged current events, neutral-current events can also be helpful in studying the non-unitarity of the mixing matrix. The important probabilities for the inclusion of the neutral current events are

$$P_{es} = 1 - (\alpha_{11}^2 (\alpha_{11}^2 + |\alpha_{21}|^2 + |\alpha_{31}|^2)); \text{ and} \quad (28)$$

$$P_{\mu s} = 1 - (\alpha_{11}^2 |\alpha_{21}|^2 + \alpha_{22}^4 + 2\alpha_{22}^2 |\alpha_{21}|^2 + \alpha_{22}^2 |\alpha_{32}|^2) \quad (29)$$

The detector cannot distinguish the various kinds of neutral current events, so we can probe the total neutral current probability:

$$P_{es} + P_{\mu s} = 2 - (\alpha_{11}^2 (\alpha_{11}^2 + 2|\alpha_{21}|^2 + |\alpha_{31}|^2) + \alpha_{22}^2 (\alpha_{22}^2 + 2|\alpha_{21}|^2 + |\alpha_{32}|^2)). \quad (30)$$

The capability of nuSTORM to probe the non unitarity parameters  $\alpha_{11}$ ,  $|\alpha_{21}|$  and  $\alpha_{22}$  are shown in Fig.6. Each plot presents 3 cases for 3 different baselines: 100 m; 1 km; and 2 km, plotted with magenta, green and blue curves respectively. The first plot in fig.6 presents the sensitivity of nuSTORM to the parameter  $\alpha_{11}$ , with the diagonal parameters  $\alpha_{22} = \alpha_{33} = 1.0$  and the off-diagonal parameters  $|\alpha_{21}|, |\alpha_{31}|$  and  $|\alpha_{32}|$  fixed at 0.01. Unitarity requires that the parameters be set to zero. However, the value of -0.01 has been drawn so that a contribution from the  $\nu_e \rightarrow \nu_\mu$  channel remains. Beginning with the first case, which shows the  $\chi^2$  as a function of  $\alpha_{11}$ , under the condition that the parameters  $|\alpha_{21}| = 0.1$  and  $\alpha_{22} = 1.0$ . The true data have been generated keeping  $\alpha_{11}$  fixed at unity while the test data have been generated

### nuSTORM Non-Unitarity

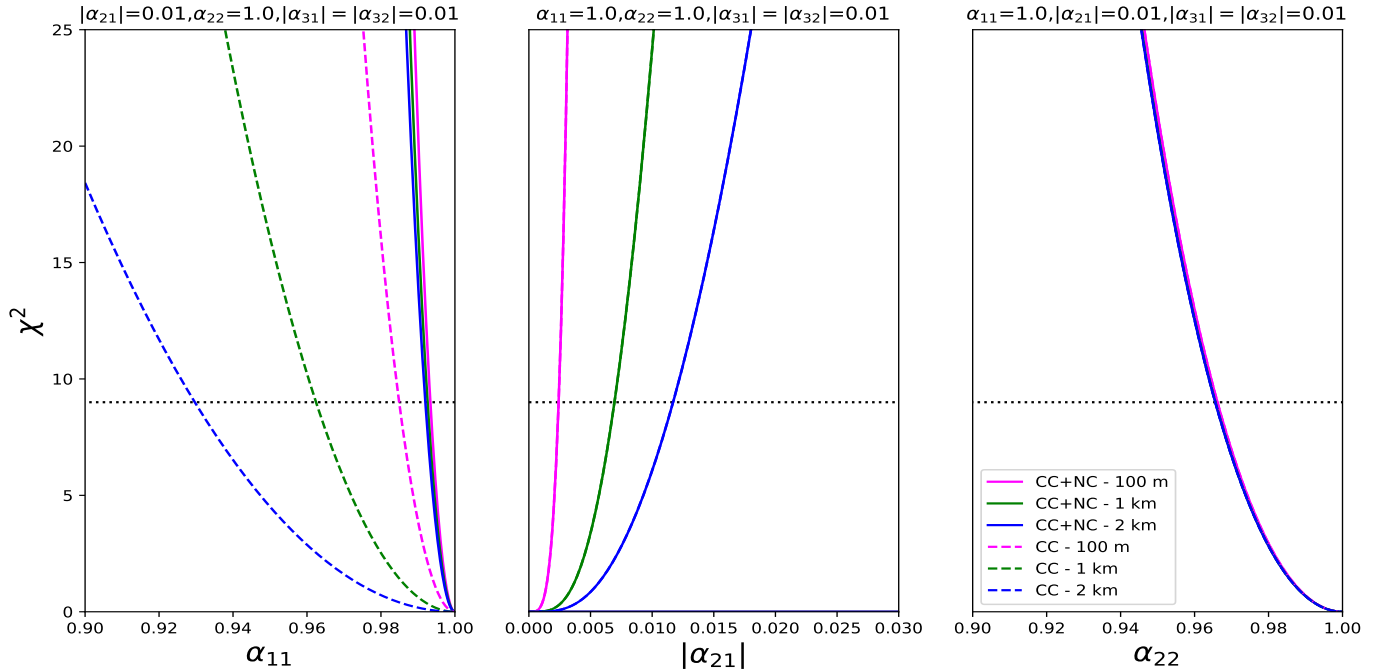


FIG. 6: The figure shows the sensitivity to nuSTORM for the non unitarity parameters  $\alpha_{11}$ ,  $|\alpha_{21}|$  and  $\alpha_{22}$ . The y-axis in the plots represent  $\chi^2$ , while the x-axis denotes  $\alpha_{11}$ ,  $|\alpha_{21}|$  and  $\alpha_{22}$  for plots respectively. In each plot the dashed lines are for the contribution of only charge current interactions while the solid lines are for the combination of charge current and neutral current. The magenta, green and blue curves represent the sensitivities at the baseline of 100 m, 1 km and 2 km respectively.

by varying  $\alpha_{11}$  between 0.9 and 1.0 while keeping all other parameters fixed. The relevant channel to study the  $\alpha_{11}$  sensitivity is the  $P_{e\mu}$  appearance channel because the probability  $P_{\bar{\mu}\bar{\mu}}$  is independent of  $\alpha_{11}$ . Under the above conditions  $P_{e\mu} \sim 0.01\alpha_{11}^2$ , therefore, the sensitivity plot has a quadratic dependence on  $\alpha_{11}$ . From the expression it is clear that  $P_{e\mu}$  is independent of the baseline so a change in sensitivity to  $\alpha_{11}$  by varying the baseline is due to the change in the flux which occurs due to the change in the baseline. Hence, we observe that the sensitivity increases as the baseline is reduced.  $3\sigma$  sensitivity for  $\alpha_{11}$  is achieved for  $\alpha_{11} = 0.93$  for a 2 km baseline, which increases to 0.96 for the 1 km baseline and the best result is achieved for the 100 m baseline where the same sensitivity is achieved

for  $\alpha_{11} = 0.99$ . If neutral current events are also combined with the charged current events a substantial improvement in the sensitivity is observed.  $3\sigma$  sensitivity for  $\alpha_{11} = 0.995$  when CC and NC both are taken into consideration. Similar studies have been performed at DUNE and T2HK [40] where the  $3\sigma$  sensitivity for  $\alpha_{11} \approx 0.94$  for DUNE and  $\alpha_{11} \approx 0.96$  for T2HK. Therefore, we can see that nuSTORM with 2 km baseline has sensitivity similar to DUNE and with baseline 1 km has similar sensitivity to T2HK when the baseline is decreased further the sensitivity increases further exceeding the sensitivities attained by DUNE or T2HK.

The second plot in the Fig.6 shows the  $\chi^2$  vs  $|\alpha_{21}|$  sensitivity with both the non-unitarity parameters  $\alpha_{11}$  and  $\alpha_{22}$  taken to be unity. Under such conditions  $P_{e\mu}$  just reduces to  $|\alpha_{21}|^2$  and  $P_{\bar{\mu}\bar{\mu}}$  becomes  $(1 + |\alpha_{21}|^2)^2$  which can be approximated to be  $\sim 1 + 2|\alpha_{21}|^2$ . Unlike the case discussed above, where only the appearance channel contributes, both the appearance and the disappearance channel contribute to the sensitivity to  $|\alpha_{21}|$ . Since both the channels depend on  $|\alpha_{21}|^2$  we get a quadratic dependence of the  $\chi^2$  on  $|\alpha_{21}|$ . In this case the true data have been generated at  $\alpha_{11} = \alpha_{22} = \alpha_{33} = 1.0$ ,  $|\alpha_{21}| = |\alpha_{31}| = |\alpha_{32}| = 0$  and  $\alpha_{22} = 1.0$ , the test data have been generated with  $|\alpha_{21}|$  varying in the range 0.0 to 0.01. In this case also we find that the sensitivity is dependent on the baseline for the same reason as discussed previously. The  $|\alpha_{21}|$  sensitivity reaches  $3\sigma$  for  $|\alpha_{21}| = 0.011$  at the 2 km baseline,  $|\alpha_{21}| = 0.006$  at the baseline 1 km, and  $|\alpha_{21}| = 0.003$  at the baseline 100 m. Neutral current events do not contribute to the  $|\alpha_{21}|$  sensitivity, this is because  $P_{NC} \approx 2 - (\alpha_{11}^2 + \alpha_{22}^2)(\alpha_{11}^2 + 2|\alpha_{21}|^2 + |\alpha_{31}|^2)$  where  $(\alpha_{11}^2 + 2|\alpha_{21}|^2 + |\alpha_{31}|^2) \approx 1$  as a result the NC channel cannot probe  $|\alpha_{21}|$  independently. Comparing the sensitivities with DUNE and T2HK [40] we observe that nuSTORM can reach  $3\sigma$  sensitivity for  $|\alpha_{21}|$  for an order of magnitude smaller values of  $|\alpha_{21}|$ . nuSTORM has a significant advantage over DUNE and T2HK which can reach  $3\sigma$  sensitivities for  $|\alpha_{21}| = 0.08$  and 0.04 respectively.

The third figure presents the sensitivity to the parameter  $\alpha_{22}$ .  $P_{e\mu}$  is independent of  $\alpha_{22}$  but  $P_{\bar{\mu}\bar{\mu}}$  is sensitive to  $\alpha_{22}$ . The true data has been generated by considering unitary evolution i.e.  $\alpha_{11} = 1.0$ ,  $|\alpha_{21}| = 0$  and  $\alpha_{22} = 1.0$  which reduces  $P_{\bar{\mu}\bar{\mu}}$  to  $\alpha_{22}^4$ . The test data have been generated by taking  $\alpha_{11} = 1.0$ ,  $|\alpha_{21}| = 0$  and varying  $\alpha_{22}$  from 0.9 to 1.0. An interesting feature observed here is the independence of  $\alpha_{22}$  on the baseline. This can be attributed to the fact that the sensitivity is solely dependent on the disappearance channel which already

has enough statistics at 2 km, hence reducing the baseline does not help. The introduction of neutral current events is expected to increase the  $\alpha_{22}$  sensitivity because of the dependence of  $P_{NC}$  on  $\alpha_{22}^2$ . However, no improvement is observed because the introduction of the channel increases the statistics but it already had enough statistics from the disappearance channel itself. The  $3\sigma$  sensitivity is reached at  $\alpha_{22} = 0.97$  for all baselines. Again from [40], the  $3\sigma$  sensitivities for DUNE and T2HK for  $\alpha_{22}$  can be attained for  $\alpha_{22} \approx 0.98$  for both the experiments.

#### IV. CONCLUSIONS

In this work we have investigated the capabilities of nuSTORM to explore two new physics scenarios – (i) the existence of eV<sup>2</sup> scale oscillation, suggested as an explanation of LSND/MiniBOONE anomalies and (ii) non-unitarity of the neutrino mixing matrix. nuSTORM is proposed primarily to measure the  $\nu_e N$  and  $\nu_\mu N$  cross sections. It was shown in [21, 22] that nuSTORM can also play an important role to study active-sterile oscillations governed by an eV<sup>2</sup> mass squared difference. In this work, we have studied the effect of including neutral current events and checked whether this can give improved sensitivity to sterile-neutrino searches. nuSTORM will have the capability to study two main channels, the conversion probability  $P_{\mu e}$  and survival probability  $P_{\bar{\mu}\bar{\mu}}$  with the proposed MIND detector. Whereas, for oscillations involving active neutrinos the NC events are not sensitive to oscillation parameters, for oscillations involving the sterile neutrinos, the neutral current events are also sensitive to the oscillation parameters through the probabilities involving conversion to sterile neutrinos  $P_{\mu s}$  and  $P_{es}$ . Considering a 2 km baseline it is observed that taking only CC interactions can constrain the mixing angle  $\theta_{24} \lesssim 7.5^\circ$ , which is better than what can be achieved with CC interactions only. For non-zero values of  $\theta_{24}$ , the constraint on  $\theta_{14}$  also improves with inclusion of NC events. Since, nuSTORM is a proposed experiment, baseline optimization is important to maximize physics output. When we consider various baselines we find that the baseline of 1 km gives a good overall sensitivity for both  $\theta_{14}$  and  $\theta_{24}$  over a wide range of  $\Delta m_{41}^2$ .

For the other new-physics scenario, non-unitarity of the lepton mixing matrix, studied in

this work, we find that nuSTORM can probe the non-unitarity parameters  $\alpha_{11}$ ,  $|\alpha_{21}|$  and  $\alpha_{22}$ .  $3\sigma$  sensitivities for  $\alpha_{11}$ ,  $|\alpha_{21}|$  and  $\alpha_{22}$  are obtained at 0.995, 0.011 and 0.97 respectively for 2 km baselines combining both CC and NC events. The sensitivities for  $\alpha_{11}$  and  $|\alpha_{21}|$  significantly improves as the baseline is reduced.

In conclusion, we find that apart from measuring neutrino cross-sections with per mil precision, nuSTORM can also contribute significantly by probing new physics scenarios beyond Standard Model .

### ACKNOWLEDGEMENTS

S. Goswami acknowledges Leverhulme Trust visiting Professorship and the hospitality at Imperial College London where the work was done. K. Chakraborty thanks the support provided by the Indo-French Centre for the Promotion of Advanced Research (IFC-PAR/CEFIPRA) for the Raman-Charpak Fellowship 2018 and the Institut Pluridisciplinaire Hubert Curien, IPHC, Strasbourg for their kind hospitality where a part of the work was completed.

- 
- [1] C. Athanassopoulos et al. Evidence for anti-muon-neutrino  $\rightarrow$  anti-electron-neutrino oscillations from the LSND experiment at LAMPF. *Phys. Rev. Lett.*, 77:3082–3085, 1996.
  - [2] A. Aguilar-Arevalo et al. Evidence for neutrino oscillations from the observation of anti-neutrino(electron) appearance in a anti-neutrino(muon) beam. *Phys. Rev.*, D64:112007, 2001.
  - [3] A. A. Aguilar-Arevalo et al. Improved Search for  $\bar{\nu}_\mu \rightarrow \bar{\nu}_e$  Oscillations in the MiniBooNE Experiment. *Phys. Rev. Lett.*, 110:161801, 2013.
  - [4] A. A. Aguilar-Arevalo et al. Significant Excess of ElectronLike Events in the MiniBooNE Short-Baseline Neutrino Experiment. *Phys. Rev. Lett.*, 121(22):221801, 2018.
  - [5] Mario A. Acero, Carlo Giunti, and Marco Laveder. Limits on nu(e) and anti-nu(e) disappearance from Gallium and reactor experiments. *Phys. Rev.*, D78:073009, 2008.

- [6] Th. A. Mueller et al. Improved Predictions of Reactor Antineutrino Spectra. *Phys. Rev.*, C83:054615, 2011.
- [7] G. Mention, M. Fechner, Th. Lasserre, Th. A. Mueller, D. Lhuillier, M. Cribier, and A. Letourneau. The Reactor Antineutrino Anomaly. *Phys. Rev.*, D83:073006, 2011.
- [8] M. Maltoni, T. Schwetz, M.A. Tortola, and J.W.F. Valle. Constraining neutrino oscillation parameters with current solar and atmospheric data. *Phys. Rev. D*, 67:013011, 2003.
- [9] Srubabati Goswami. Accelerator, reactor, solar and atmospheric neutrino oscillation: Beyond three generations. *Phys. Rev. D*, 55:2931–2949, 1997.
- [10] Xiaoyong Chu, Basudeb Dasgupta, Mona Dentler, Joachim Kopp, and Ninetta Saviano. Sterile neutrinos with secret interactions—cosmological discord? *JCAP*, 11:049, 2018.
- [11] Graciela Gelmini, Sergio Palomares-Ruiz, and Silvia Pascoli. Low reheating temperature and the visible sterile neutrino. *Phys. Rev. Lett.*, 93:081302, 2004.
- [12] Carlos E. Yaguna. Sterile neutrino production in models with low reheating temperatures. *JHEP*, 06:002, 2007.
- [13] P.F. de Salas, M. Lattanzi, G. Mangano, G. Miele, S. Pastor, and O. Pisanti. Bounds on very low reheating scenarios after Planck. *Phys. Rev. D*, 92(12):123534, 2015.
- [14] S. Gariazzo, C. Giunti, M. Laveder, and Y.F. Li. Updated Global 3+1 Analysis of Short-BaseLine Neutrino Oscillations. *JHEP*, 06:135, 2017.
- [15] Mona Dentler, Ivaro Hernandez-Cabezudo, Joachim Kopp, Pedro A.N. Machado, Michele Maltoni, Ivan Martinez-Soler, and Thomas Schwetz. Updated Global Analysis of Neutrino Oscillations in the Presence of eV-Scale Sterile Neutrinos. *JHEP*, 08:010, 2018.
- [16] Carsten Rott. Status and Prospects of the JSNS<sup>2</sup> Experiment. *PoS*, ICHEP2018:185, 2019.
- [17] Y. J. Ko et al. Sterile Neutrino Search at the NEOS Experiment. *Phys. Rev. Lett.*, 118(12):121802, 2017.
- [18] A. P. Serebrov et al. First Observation of the Oscillation Effect in the Neutrino-4 Experiment on the Search for the Sterile Neutrino. *Pisma Zh. Eksp. Teor. Fiz.*, 109(4):209–218, 2019. [JETP Lett.109,no.4,213(2019)].
- [19] Alireza Haghighat, Patrick Huber, Shengchao Li, Jonathan M. Link, Camillo Mariani, Jaewon Park, and Tulasi Subedi. Observation of Reactor Antineutrinos with a Rapidly-Deployable

- Surface-Level Detector. 2018.
- [20] I Alekseev et al. Search for sterile neutrinos at the DANSS experiment. *Phys. Lett.*, B787:56–63, 2018.
  - [21] C. D. Tunnell. Sterile Neutrino Sensitivity with Wrong-Sign Muon Appearance at nuSTORM. 2012.
  - [22] D. Adey et al. Light sterile neutrino sensitivity at the nuSTORM facility. *Phys. Rev.*, D89(7):071301, 2014.
  - [23] N. Allemandou et al. The STEREO Experiment. *JINST*, 13(07):P07009, 2018.
  - [24] R. Acciarri et al. Long-Baseline Neutrino Facility (LBNF) and Deep Underground Neutrino Experiment (DUNE). 2015.
  - [25] K. Abe et al. Physics Potentials with the Second Hyper-Kamiokande Detector in Korea. 2016.
  - [26] Steven Weinberg. Baryon and Lepton Nonconserving Processes. *Phys. Rev. Lett.*, 43:1566–1570, 1979.
  - [27] Rabindra N. Mohapatra and Goran Senjanovic. Neutrino Mass and Spontaneous Parity Non-conservation. *Phys. Rev. Lett.*, 44:912, 1980. [,231(1979)].
  - [28] Srubabati Goswami and Toshihiko Ota. Testing non-unitarity of neutrino mixing matrices at neutrino factories. *Phys. Rev.*, D78:033012, 2008.
  - [29] Werner Rodejohann. Non-Unitary Lepton Mixing Matrix, Leptogenesis and Low Energy CP Violation. *EPL*, 88(5):51001, 2009.
  - [30] Michal Malinsky, Tommy Ohlsson, and He Zhang. Non-unitarity effects in a realistic low-scale seesaw model. *Phys. Rev.*, D79:073009, 2009.
  - [31] S. Antusch, C. Biggio, E. Fernandez-Martinez, M. B. Gavela, and J. Lopez-Pavon. Unitarity of the Leptonic Mixing Matrix. *JHEP*, 10:084, 2006.
  - [32] Stefan Antusch, Mattias Blennow, Enrique Fernandez-Martinez, and Jacobo Lopez-Pavon. Probing non-unitary mixing and CP-violation at a Neutrino Factory. *Phys. Rev.*, D80:033002, 2009.
  - [33] Michal Malinsky, Tommy Ohlsson, Zhi-zhong Xing, and He Zhang. Non-unitary neutrino mixing and CP violation in the minimal inverse seesaw model. *Phys. Lett.*, B679:242–248, 2009.

- [34] Mattias Blennow, Pilar Coloma, Enrique Fernandez-Martinez, Josu Hernandez-Garcia, and Jacobo Lopez-Pavon. Non-Unitarity, sterile neutrinos, and Non-Standard neutrino Interactions. *JHEP*, 04:153, 2017.
- [35] Stefan Antusch and Oliver Fischer. Non-unitarity of the leptonic mixing matrix: Present bounds and future sensitivities. *JHEP*, 10:094, 2014.
- [36] F. J. Escrihuela, D. V. Forero, O. G. Miranda, M. Tortola, and J. W. F. Valle. On the description of nonunitary neutrino mixing. *Phys. Rev.*, D92(5):053009, 2015. [Erratum: *Phys. Rev.*D93,no.11,119905(2016)].
- [37] Debajyoti Dutta and Pomita Ghoshal. Probing CP violation with T2K, NO $\nu$ A and DUNE in the presence of non-unitarity. *JHEP*, 09:110, 2016.
- [38] Luis Salvador Miranda, Pedro Pasquini, Ushak Rahaman, and Soebur Razzaque. Searching for non-unitary neutrino oscillations in the present T2K and NO $\nu$ A data. 2019.
- [39] Andr De Gouvea, Kevin J. Kelly, G. V. Stenico, and Pedro Pasquini. Physics with Beam Tau-Neutrino Appearance at DUNE. *Phys. Rev.*, D100(1):016004, 2019.
- [40] Debajyoti Dutta and Samiran Roy. Non Unitarity at DUNE and T2HK with Charged and Neutral Current Measurements. 2019.
- [41] S. P. Behera, Anushree Ghosh, Sandhya Choubey, V. M. Datar, D. K. Mishra, and A. K. Mohanty. Search for the sterile neutrino mixing with the ICAL detector at INO. *Eur. Phys. J.*, C77(5):307, 2017.
- [42] K. Abe et al. Search for light sterile neutrinos with the T2K far detector Super-Kamiokande at a baseline of 295 km. *Phys. Rev.*, D99(7):071103, 2019.
- [43] P. Adamson et al. Search for active-sterile neutrino mixing using neutral-current interactions in NO $\nu$ A. *Phys. Rev.*, D96(7):072006, 2017.
- [44] P. Adamson et al. Active to sterile neutrino mixing limits from neutral-current interactions in MINOS. *Phys. Rev. Lett.*, 107:011802, 2011.
- [45] Raj Gandhi, Boris Kayser, Suprabh Prakash, and Samiran Roy. What measurements of neutrino neutral current events can reveal. *JHEP*, 11:202, 2017.
- [46] Justin Evans. The MINOS Experiment: Results and Prospects. *Adv. High Energy Phys.*, 2013:182537, 2013.

- [47] Patrick Huber, M. Lindner, and W. Winter. Simulation of long-baseline neutrino oscillation experiments with GLOBES. *Comput. Phys. Commun.*, 167:195, 2005.
- [48] Patrick Huber, Joachim Kopp, Manfred Lindner, Mark Rolinec, and Walter Winter. New features in the simulation of neutrino oscillation experiments with GLOBES 3.0. *Comput. Phys. Commun.*, 177:432–438, 2007.
- [49] NuFIT 4.1. [www.nu-fit.org](http://www.nu-fit.org), 2019.
- [50] Ivan Esteban, M. C. Gonzalez-Garcia, Alvaro Hernandez-Cabezudo, Michele Maltoni, and Thomas Schwetz. Global analysis of three-flavour neutrino oscillations: synergies and tensions in the determination of  $\theta_{23}$ ,  $\delta_{CP}$ , and the mass ordering. 2018.
- [51] J.-B. Lagrange. Neutrinos from stored muons, nustorm. *Nuclear and Particle Physics Proceedings*, 273-275:1771 – 1776, 2016. 37th International Conference on High Energy Physics (ICHEP).
- [52] Pilar Coloma, David V. Forero, and Stephen J. Parke. DUNE Sensitivities to the Mixing between Sterile and Tau Neutrinos. *JHEP*, 07:079, 2018.